Chinese Chemical Letters 33 (2022) 1070–1073

Contents lists available at ScienceDirect

Chinese Chemical Letters

journal homepage: www.elsevier.com/locate/cclet

Single-atomic Fe anchored on hierarchically porous carbon frame for efficient oxygen reduction performance

Yaling Jia, Fangshuai Zhang, Qinglin Liu, Jun Yang, Jiahui Xian, Yamei Sun, Yinle Li, Guangqin Li*

MOE Laboratory of Bioinorganic and Synthetic Chemistry, Lehn Institute of Functional Materials, School of Chemistry, Sun Yat-sen University, Guangzhou 510275, China

ARTICLE INFO

Article history:
Received 29 April 2021
Revised 18 May 2021
Accepted 24 May 2021
Available online 29 May 2021

Keywords:
Single atom Fe
High atom utilization
Efficient mass transfer
Oxygen reduction reaction
Zinc-air battery
Efficient performance

ABSTRACT

Exploring platinum group metal-free electrocatalysts with superior catalytic performance and favorable durability for oxygen reduction reaction is a remaining bottleneck in process of developing sustainable techniques in energy storage and conversion. Herein, a hierarchical porous single atomic Fe electrocatalyst (Fe/Z8-E-C) is rationally designed and synthesized *via* acid etching, calcination, adsorption of Fe precursor and recalcination processes. This unique electrocatalyst Fe/Z8-E-C shows excellent oxygen reduction performance with a half-wave potential of 0.89 V in 0.1 mol/L KOH, 30 mV superior to that of commercial Pt/C (0.86 V), which is also significantly higher than that of typical Fe-doped ZIF-8 derived carbon nanoparticles (Fe/Z8-C) with a half-wave potential of 0.84 V. Furthermore, Fe/Z8-E-C-based Zn-air battery exhibits greatly enhanced peak power density and specific capacity than those of original Fe/Z8-C, verifying the remarkable performance and practicability of this specially designed hierarchical structure due to its efficient utilization of the active sites and rapid mass transfer. This present work proposes a new method to rationally synthesize single atom electrocatalysts loaded on hierarchical porous frame materials for catalysis and energy conversion.

With the depletion of fossil energy and their accompanying detrimental effects on environment, it is urgent to replace traditional fossil fuels with sustainable energies [1,2]. Therefore, developing advanced sustainable energy conversion techniques, such as proton exchange membrane fuel cells, polymer electrolyte fuel cells and Zn-air batteries, is proceeding rapidly. As cathode reaction for fuel cells and metal air batteries, oxygen reduction reaction (ORR) is kinetically sluggish [3]. Platinum (Pt) possesses the highest kinetic activity as the benchmark electrocatalyst for ORR [4–6], while its high cost comprises a large part of fuel cells expense [7]. Thus, the accomplishment of efficient and durable noble metal-free ORR catalysts is crucially important for commercialization of fuel cell-powered vehicles [8–10]. Despite a number of transition metal-based ORR electrocatalysts or metal-free carbon materials [11], such as chalcogenides [12,13], nitrides [14,15], molecular electrocatalyst [16] and conducting MOFs/polymers [17], have been reported, their performance need to be further improved owing to their limited intrinsic activity and insufficient exposed active sites.

Among non-precious based ORR electrocatalysts, single atoms catalysts (SACs), with isolated active sites homogeneously dispersed on an appropriate support, have aroused enormous attention by virtue of their maximum atom efficiency and high catalytic activity [18–24]. Most of them are anchored on carbon materials derived from polymers [25,26], molecules [27], supramolecular species [28] and biomacromolecules [4,5,27,29–36]. Benefitting from the adjustable electronic structure of SACs, many previous works predominately focused on improving electrocatalytic performance *via* fabricating the coordination environment or increasing metal loading of SACs [18,37–40]. However, the high metal loading made SACs prone to migration and aggregation to form nanoparticles due to their high surface free energy [41]. Consequently, exploring an appropriate matrix with ultrahigh surface area and strong interaction with single atoms is a vital step to ensure their activity and stability during catalysis.

Metal organic frameworks (MOFs), featured with high specific surface area, adjustable chemical components, and surface functionality, are incredible platforms for MOFs-derived electrocatalyst [42–44]. Recently, MOF derived carbon-based electrocatalysts with high electrical conductivity and uniformly distributed active sites have emerged as promising alternatives to Pt for ORR [45–50], and

* Corresponding author.
E-mail address: liguangqin@mail.sysu.edu.cn (G. Li).

https://doi.org/10.1016/j.cclet.2021.05.052
1001-8417/

also as excellent support for metal single atom electrocatalyst [51–53]. Impressively, ZIF-8 as a typical host to prepare carbon materials comprising the metal/nitrogen coordinated active centers demonstrates potential as ORR electrocatalyst [54]. However, the micropores within them are easily blocked by the produced H_2O and then lose their capacity to adsorb O_2, which fails to meet the need of rapid mass transfer [4,55,56]. Especially in the real condition of fuel cells or Zn-air battery, the electrode could not rotate rapidly like the rotating disk in the ORR test, which certainly will further restrict the practicability of the ORR electrocatalysts.

In this research, a hierarchical porous structure decorated with single Fe atom sites has been prepared *via* a template-free method by firstly acid etching ZIF-8 and sintering, then introducing Fe precursor and secondly sintering (named as Fe/Z8-E-C). However, other hierarchical porous materials are usually derived from MOFs by additional templates, such as employing polystyrene sphere, silica and so on. Interestingly, the half-wave potential of the obtained Fe/Z8-E-C reaches to 0.89 V in alkaline solution, and surpasses those of contrastive sample without etching, Pt/C and many other reported catalysts. This excellent ORR catalytic activity is attributed to the special hierarchically nanostructure, which not only avoids agglomeration of single atom metal sites but favors mass transfer of ORR-related species and increases the single atom utilization. Moreover, the activity and stability of Fe/Z8-E-C were further studied in a homemade zinc-air battery, and the results verified its practicability and favorable performance. This work rationally increases atom utilization by loading single atom Fe on a hierarchical porous structure employing a template-free method.

The synthesis process of Fe/Z8-E-C with hierarchical porous structure and efficient mass transfer was briefly illustrated in Fig. S1 (Supporting information). Firstly, ZIF-8 was synthesized and etched based on acid-base reaction to form macroporous ZIF-8 (ZIF-8-E). Powder X-ray diffraction (PXRD) and scanning electron microscopy (SEM) confirmed the successful preparation of macroporous ZIF-8-E with similar crystal structure to that of original ZIF-8 (Figs. S2-S4 in Supporting information). N_2 adsorption-desorption isotherms of ZIF-8 and ZIF-8-E at 77 K (Fig. S5 in Supporting information) showed that the Brunauer–Emmett–Teller (BET) surface area of ZIF-8-E (1755 m^2/g) is lower than that of original ZIF-8 (1833 m^2/g) (Table S1 in Supporting information), which reflects the formation of macropores. Subsequently, macroporous ZIF-8-E was preheated at 800 °C to form a hierarchical framework to absorb the iron source TPI ions $([Fe(Phen)_3])^{2+}$ (a Fe(II) phenanthroline complex) [38]. Finally, the integrated precursor was pyrolyzed in argon to obtain Fe/Z8-E-C. The adsorbed TPI and preheated ZIF-8 host decomposed simultaneously in the subsequent high-temperature pyrolysis (Fig. S6 in Supporting information), which favors the *in situ* generation of homogeneous dispersed single atomic Fe without metal agglomeration, as confirmed by XRD, transmission electron microscopy (TEM) and elemental mappings (Figs. S7-S9 in Supporting information). During process of performance optimization, the preheating temperature in the second step was adjusted from 700 °C to 900 °C and the amount of Fe content was regulated by varying the amount of precursor TPI to target corresponding products (Fig. S10 in Supporting information), and the specific synthesis process was indicated in Supporting information.

The carbonized Fe/Z8-E-C was characterized by SEM. In Fig. 1a, Fe/Z8-E-C displays a frame-like morphology with a macropore about 130 nm, opening a new window for reactants channels. N_2 adsorption–desorption isotherms (Fig. S11 and Table S1 in Supporting information) demonstrate that the BET surface area of Fe/Z8-E-C is lower than that of Fe/Z8-C, further confirming the existence of macropores in the Fe/Z8-E-C and displaying consistentence with SEM image. The detailed pore size distribution reflects that the carbon framework of Fe/Z8-E-C possesses abundant pore structures of micropores and mesopores. The SEM image coupled with N_2 adsorption-desorption experiment results suggest the unique hierarchically super-macroporous strucutre of Fe/Z8-E-C may be a potential catalyst. The annular bright-field scanning transmission electron microscopy images were presented in Figs. 1b and c, where no agglomeration metal particle was detected. Elemental mapping images (Fig. 1d) of nano-hollow box reveals the homogeneous distribution of Fe throughout the particle, implying the atomically dispersed Fe in Fe/Z8-E-C [57]. The Fe element content in Fe/Z8-E-C and Fe/Z8-C determined by energy dispersive X-ray spectroscopy were 0.34% and 0.65%, respectively (Table S2 in Supporting information). The Fe content ratio is in consistency with that of determined by inductively coupled plasma mass spectroscopic (ICP-MS) measurements (Table S3 in Supporting information). The spherical aberration corrected HAADF-STEM was conducted to detect the single atoms. The bright dots circled red in Fig. 1e represent the Fe single atom species. Only two broad diffraction peaks at about 26° and 44°, which were assigned to (002) and (101) planes of graphite, respectively, were observed in the PXRD pattern of Fe/Z8-E-C (Fig. 1f) [58]. No diffraction peaks of Fe nanoparticles appeared in the XRD pattern, which is consistent with TEM results. X-ray photoelectron spectroscopy (Fig. S12 in Supporting information) was also employed to investigate the existence form of element N and Fe. N 1s high-resolution spectrum (Fig. S13a in Supporting information) of Fe/Z8-E-C was deconvoluted into several peaks corresponding to graphitic N (401.4 eV), pyrrolic nitrogen (400.1 eV), and pyridinic nitrogen (398.4 eV) [59–61]. Fe 2p high-resolution spectrum of Fe/Z8-E-C (Fig. S13b in Supporting information) demonstrated two peaks located at 709.7 and 724.6 eV, which could be assigned to Fe $2p_{3/2}$ and $2p_{1/2}$ orbitals of Fe^{3+}, respectively [62,63].

To further verify the exsitence form of single atom Fe, Fe K-edge X-ray absorption near edge structure (XANES) (Fig. 2a) was used to investigate the oxidation state of Fe single atom in hierarchically porous carbon material. As shown in the Fe K-edge XANES spectrum of Fe/Z8-E-C catalyst and standard compounds, Fe K-edge

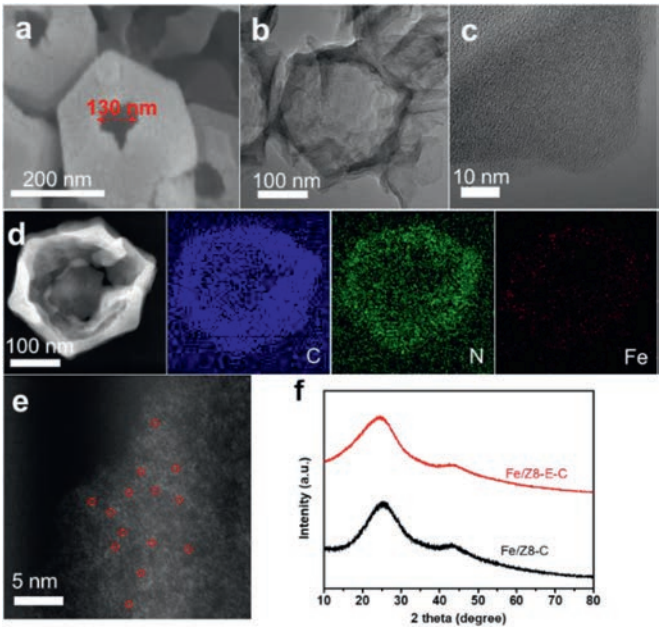

Fig. 1. (a) SEM image of Fe/Z8-E-C. (b, c) STEM images of Fe/Z8-E-C. (d) HAADF-STEM images of Fe/Z8-E-C and EDS elemental mappings of C (blue), N (green), Fe (red). (e) High-angle annular dark-filed scanning transmission electron microscopy (HAADF-STEM) image of Fe/Z8-E-C. (f) XRD patterns of Fe/Z8-C and Fe/Z8-E-C.

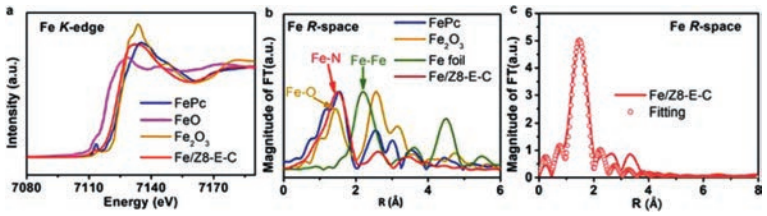

Fig. 2. (a) Normalized Fe K-edge XANES spectra, (b) Fourier transform Fe K-edge EXAFS spectra and (c) EXAFS fitting results of Fe/Z8-E-C.

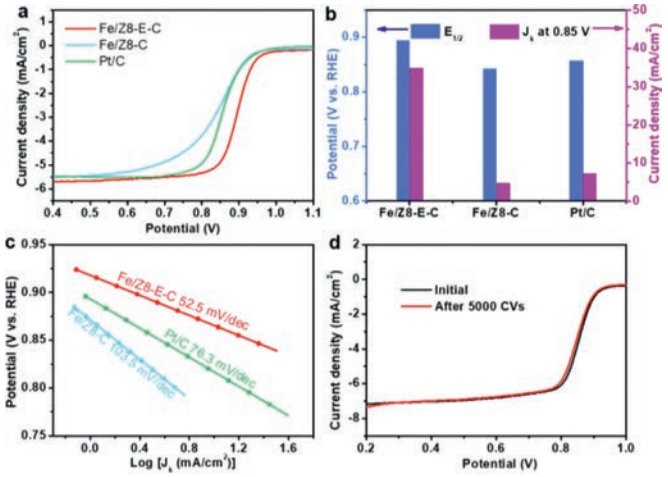

Fig. 3. (a) LSV curves for different catalysts in O_2 saturated 0.1 mol/L KOH solution with a rotating speed of 1600 rpm at a scan rate of 10 mV/s. (b) Corresponding half-wave potentials and kinetic current densities at 0.85 V. (c) Tafel plots of Fe/Z8-E-C, Fe/Z8-C and Pt/C. (d) LSV curves of Fe/Z8-E-C before and after 5000 CVs.

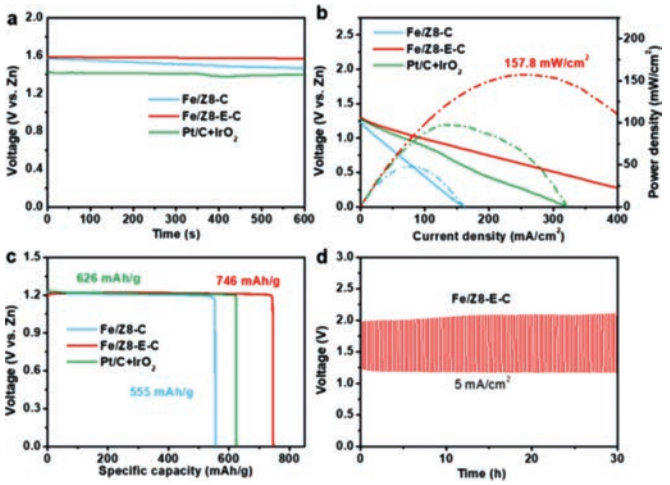

Fig. 4. (a) Initial open-circuit potentials of Zn-air batteries with Fe/Z8-E-C, Fe/Z8-C and Pt/C-IrO_2 as the air cathode catalysts, respectively. (b) Polarization curves and corresponding power density plots of Zn-air batteries with Fe/Z8-E-C, Fe/Z8-C and Pt/C-IrO_2 as the air electrode catalysts. (c) The specific capacities of Fe/Z8-E-C, Fe/Z8-C and Pt/C-IrO_2. (d) Discharge-charge cycling curves of Fe/Z8-E-C at 5 mA/cm^2 for 90 cycles.

pre-edge absorption energy position of Fe/Z8-E-C was between FeO and Fe_2O_3, which demonstrates that the valence state of Fe single atoms is close to +3. Besides, extended X-ray absorption fine structure (EXAFS) analysis was carried out to investigate the local environment of Fe sites. The Fourier transform of k^3-weighted Fe K-edge EXAFS spectra (Fig. 2b) revealed a main peak at about 1.55 Å close to that of Fe-Pc (1.57 Å) which is ascribed to Fe-N configureuration from first coordination shell [64,65]. The absence of peak at 2.2 Å in the FT-EXAFS spectra of Fe/Z8-E-C confirms the absence of Fe–Fe interactions, further certifying the existence of atomically dispersed Fe sites on the carbon frame material which coincides to the HAADF-STEM results. Furthermore, Fig. 2c presents EXAFS R-space fitting curve of Fe/Z8-E-C and corresponding parameters were shown in Table S4 (Supporting information). The fitting result showed that atomically dispersed Fe sites existed in the form of FeN_4 coordination structure in Fe/Z8-E-C [53,66,67].

As mentioned above, possessing the hierarchically porous structure and single atom Fe-N_4 sites, the catalyst Fe/Z8-E-C is supposed to exhibit expectative ORR performance. At first, cyclic voltammetry (CV) measurement was conducted in Ar- and O_2-saturated alkaline solution of 0.1 mol/L KOH, respectively. As can be seen in Fig. S14 (Supporting information), compared with the curves in N_2-saturated electrolyte solution, obvious cathode peaks appeared in O_2-saturated electrolyte, indicating that the oxygen redution process occurs. The more positive position of Fe/Z8-E-C than that of Pt/C implies its efficient performance. Additionally, linear sweep voltammetry (LSV) curves in O_2-saturated 0.1 mol/L KOH were collected to evaluate the ORR performance. As shown in Figs. 3a and b and Table S5 (Supporting information), Fe/Z8-E-C exhibited a more positive half-wave potential ($E_{1/2}$, 0.89 V *vs.* RHE) and a higher kinetic current density than Fe/Z8-C and Pt/C, evidencing the specific open frame-like structure promoting the mass transfer and benefitting the accessibility of electrolyte to inner exposed active sites [68]. The excellent performcance is also superior than many previously reported ORR electrocatalyts (Table S6 in Supporting information). Fig. S15a (Supporting information) compares the ORR activity of carbon matrixes without loading Fe single atom, which verifies this hierachical structure advantage again. Fig. 3c and Fig. S15b (Supporting information) show the corresponding Tafel slopes of catalysts, Fe/Z8-E-C possesses the smallest Tafel slope of 52.5 mV/dec among these catalysts, indicating a high intrinsic activity and a faster reaction kinetics of Fe/Z8-E-C. Koutecky–Levich (K–L) plots (Fig. S16 in Supporting information) and rotating-ring-disk-electrode measurements (Fig. S17 in Supporting information) both revealed that the electron transfer number (n) of Fe/Z8-E-C was about 4.0, indicating an efficient 4e$^-$ pathway. Additionally, after 5000 cycles (Fig. 3d), the $E_{\text{on-set}}$ potential for Fe/Z8-E-C exhibits a negligible change and only a slight decrease of limited diffusion current density, suggesting that Fe single atom loaded on porous frame-like carbon is equipped with excellent durability. Besides, TOF value of Fe/Z8-E-C is 14 times higher than that of Fe/Z8-C (Table S3). Coupled with the quantitative results of Fe content, the high TOF value reveal a higher atomic utilization efficiency of Fe for Fe/Z8-E-C and the rapid mass transfer of this rationally designed nanostructure, which enhances accessibility of active sites with reaction intermediates [69,70].

To evaluate the practicability of this electrocatalyst, a homemade Zn-air battery was assembled and tested in ambient condition. As shown in Fig. 4a, a higher open circuit potential of 1.58 V from Fe/Z8-E-C-based battery was exhibited than those of Fe/Z8-C and Pt/C, respectively. Fig. 4b shows the discharge polarization curves and corresponding power density curves. The peak power

density of the Fe/Z8-E-C-based battery reaches 157.8 mW/cm^2 at 254.9 mA/cm^2, which is significantly higher than those of Fe/Z8-C, Pt/C-based batteries, and many other reported non-precious metal-based electrocatalysts assembled Zn-air batteries (Table S7 in Supporting information). In Fig. 4c, the specific capacity of Fe/Z8-EC-based battery delivers 746 mAh/g which is the best among these homemade batteries. Galvanostatic cyclings of Zn–air batteries (Fig. 4d) were conducted to evaluate the recharge-ability of Fe/Z8-E-C-based battery, in which only a small increase of battery charge-discharge volatage gap at 5 mA/cm^2 for 30 h was observed. This excellent performance and robust stability for Fe/Z8-E-C as cathode material further confirmed the outstanding ORR performance of this rationally designed nanostructure and revealed its high application value.

In summary, an efficient single isolated Fe atoms electrocatalyst loaded on hierarchically porous carbon frame (Fe/Z8-E-C) has been rationally synthesized for ORR. Owing to the morphological advantage of hierachical nanostructure and high atom utilization, the catalyst Fe/Z8-E-C achieves a superior half-wave potential of 0.89 V than those of control sample Fe/Z8-C and commercial Pt/C. More importantly, it shows a remarkable performance in Zn-air battery as air electrode catalyst, achieving a high capacity of 746 mAh/g and an ultrahigh peak power density of 157.8 mW/cm^2. The outstanding performance resuts from contiguous trimodal pore distribution of this open-pore nanostructure which provides reactants channels and exposes more active sites in favor of efficient mass transfer. In addition, this work also expands the strategies to bulid more reactants channels and enhance atom utilization for accessibility of active sites with reaction intermediates in oxygen reduction process.

Declaration of competing interest

The authors declare no conflict of competing interest.

Acknowledgments

This work was supported by National Key R&D Program of China (No. 2018YFA0108300), the Overseas High-level Talents Plan of China and Guangdong Province, the Fundamental Research Funds for the Central Universities, the 100 Talents Plan Foundation of Sun Yat-sen University, the Program for Guangdong Introducing Innovative and Entrepreneurial Teams (No. 2017ZT07C069), and the Natinoal Natural Science Foundation of China (Nos. 22075321, 21821003, 21890380 and 21905315).

Supplementary materials

Supplementary material associated with this article can be found, in the online version, at doi:10.1016/j.cclet.2021.05.052.

References

[1] D. Yan, L. Dai, S. Wang, et al., Adv. Mater. 29 (2017) 1606459.
[2] E. Luo, C.H. Choi, C. Liu, W. Xing, Energy Environ. Sci. 14 (2021) 2158–2185.
[3] Q. Wang, Y. Li, S. Wang, et al., ACS Energy Lett. 3 (2018) 1183–1191.
[4] J. Li, L. Li, Z. Wei, et al., Angew. Chem. Int. Ed. 58 (2019) 7035–7039.
[5] K. Yuan, Y. Chen, U. Scherf, et al., J. Am. Chem. Soc. 142 (2020) 2404–2412.
[6] A. Kulkarni, A. Patel, J.K. Nørskov, et al., Chem. Rev. 118 (2018) 2302–2312.
[7] X.X. Wang, M.T. Swihart, G. Wu, et al., Nat. Catal. 2 (2019) 578–589.
[8] P. Song, Z. Jiang, L. Gu, et al., Adv. Funct. Mater. 27 (2017) 1700802–1700807.
[9] A.A. Gewirth, J.A. Varnell, A.M. DiAscro, Chem. Rev. 118 (2018) 2313–2339.
[10] E.I. Solomon, S.S. Stahl, Chem. Rev. 118 (2018) 2299–2301.
[11] Y. Zhang, L. Tao, S. Wang, et al., Adv. Mater. 32 (2020) 1905923.
[12] H.M. Zhang, C. Zhu, J. Xu, et al., Chem. Eng. J. 375 (2019) 122058.
[13] J.H. Kim, Y. Choi, M. Liu, et al., Energy Environ. Sci. 14 (2021) 1506–1516.
[14] J. Luo, H. Song, S. Liao, et al., ACS Catal. 6 (2016) 6165–6174.
[15] M.E. Kreider, L.A. King, T.F. Jaramillo, et al., Chem. Mater. 32 (2020) 2946–2960.
[16] R. Cao, M. Liu, J. Cho, et al., Nat. Commun. 4 (2013) 2076.
[17] S.S. Shinde, S.U. Lee, J.H. Lee, et al., Energy Environ. Sci. 12 (2019) 727–738.
[18] Y. Zhao, Q. He, J. Liu, et al., ACS Appl. Mater. Inter. 12 (2020) 17334–17342.
[19] L. Jiao, S.H. Yu, H.L. Jiang, et al., Nat. Commun. 11 (2020) 2831.
[20] X. Fu, A. Yu, Z. Chen, et al., Adv. Energy Mater. 9 (2019) 1803737.
[21] L. Gong, C. Liu, W. Xing, et al., Angew. Chem. Int. Ed. 59 (2020) 13923–13928.
[22] X. Yang, L. Gan, J. Li, et al., Adv. Sci. 7 (2020) 2000176.
[23] Y. Zhu, Y. Mei, G. Wu, et al., Adv. Energy Mater. 10 (2020) 1902844.
[24] K. Kumar, F. Maillard, L. Dubau, et al., ACS Catal. 11 (2021) 484–494.
[25] X. Wei, Y. Zhao, G. Zhang, et al., Angew. Chem. Int. Ed. 59 (2020) 14639–14646.
[26] H. Zhang, Z. Li, X.W. Lou, et al., Energy Environ. Sci. 11 (2018) 1980–1984.
[27] Z. Zhang, J. Sun, L. Dai, et al., Angew. Chem. Int. Ed. 57 (2018) 9038–9043.
[28] J. Xie, Z.W. Zhang, Q. Zhang, et al., Angew Chem. Int. Ed. 58 (2019) 4963–4967.
[29] I.A. Choi, J.E. Won, K.W. Park, et al., Appl. Catal. B 211 (2017) 235–244.
[30] M. Qiao, S. Zhang, S. Wang, et al., Angew. Chem. Int. Ed. 59 (2020) 2688–2694.
[31] Z. Yang, X. Duan, Y. Wu, et al., Nat. Commun. 10 (2019) 3734.
[32] Z. Wang, Y. Xiong, S. Mu, et al., Adv. Funct. Mater. 28 (2018) 1802596.
[33] Y. Qu, Y. Wu, Y. Li, et al., Nat. Catal. 1 (2018) 781–786.
[34] I.S. Amiinu, H. Zhang, S. Mu, et al., Adv. Funct. Mater. 28 (2018) 1704638.
[35] J. Li, Z. Wang, G. Wu, et al., Nat. Catal. 1 (2018) 935–945.
[36] H.T. Chung, K.L. More, P. Zelenay, et al., Science 357 (2017) 479.
[37] H. Yang, G. Lu, Z. Liu, et al., Appl. Catal. B 278 (2020) 119270.
[38] X. Wan, M. Xu, J. Shui, et al., Nat. Catal. 2 (2019) 259–268.
[39] C.C. Hou, J. Yu, Q. Xu, et al., Angew. Chem. Int. Ed. 59 (2020) 7384–7389.
[40] F. Wu, L. Mao, Y. Li, et al., J. Am. Chem. Soc. 142 (2020) 16861–16867.
[41] L. Jiao, H.L. Jiang, Chem 5 (2019) 786–804.
[42] Y. Chen, D. Wang, Y. Li, et al., Angew. Chem. Int. Ed. 56 (2017) 6937–6941.
[43] Z. Xue, K. Liu, G. Li, et al., Nat. Commun. 10 (2019) 5048.
[44] Y. Chen, D. Wang, Y. Li, et al., Angew. Chem. Int. Ed. 60 (2021) 3212–3221.
[45] X.F. Lu, B.Y. Xia, X.W.D. Lou, et al., Angew Chem. Int. Ed. 59 (2020) 4634–4650.
[46] Y. Lei, Y. Si, H. Wang, et al., J. Mater. Chem. A 8 (2020) 20629–20636.
[47] Z. Zhu, H. Yin, H. Zhao, et al., Adv. Mater. (2020) 2004670.
[48] C.C. Hou, L. Zou, Q. Xu, Adv. Mater. 31 (2019) 1904689.
[49] N. Larouche, R. Chenitz, J.P. Dodelet, et al., Electrochim. Acta 115 (2014) 170–182.
[50] F. Jaouen, V. Goellner, J.P. Dodelet, et al., Electrochim. Acta 87 (2013) 619–628.
[51] A. Indra, T. Song, U. Paik, Adv. Mater. 30 (2018) 1705146.
[52] T. Wang, Z. Kou, F. Verpoort, et al., Adv. Funct. Mater. 28 (2018) 1705048.
[53] S. Lee, S. Oh, M. Oh, Angew. Chem. Int. Ed. 59 (2020) 1327–1333.
[54] A. Zitolo, E. Fonda, F. Jaouen, et al., Nat. Mater. 14 (2015) 937–942.
[55] E. Proietti, J. Herranz, J.P. Dodelet, Nat. Commun. 2 (2011) 416.
[56] X. Wang, G. Wu, X. Li, et al., Nano Energy 25 (2016) 110–119.
[57] J. Gu, H.M. Chen, X. Hu, et al., Science 364 (2019) 1091.
[58] L. Fan, S. Qiu, X. Yao, et al., Nat. Commun. 7 (2016) 10667.
[59] S. Chen, C. Zhi, J.A. Zapien, Adv. Funct. Mater. 30 (2020) 1908945.
[60] X.R. Wang, S.Z. Qiao, J. Yang, Adv. Mater. 30 (2018) 1800005.
[61] N. Zhang, C. Wu, Y. Xie, Energy Environ. Sci. 13 (2020) 111–118.
[62] J. Yang, Y. Xiong, H. Xu, Adv. Funct. Mater. 27 (2017) 1606497.
[63] Z. Huang, H. Li, Y. Kuang, ACS Nano 12 (2018) 208–216.
[64] H. Fei, X. Duan, Y. Huang, Nat. Catal. 1 (2018) 63–72.
[65] R. Jiang, Y. Chen, L. Wang, J. Am. Chem. Soc. 140 (2018) 11594–11598.
[66] M. Zhang, D. Wang, Y. Li, J. Am. Chem. Soc. 139 (2017) 10976–10979.
[67] G. Wu, C.M. Johnston, P. Zelenay, et al., Science 332 (2011) 443.
[68] J. Nai, X.W.D. Lou, Adv. Mater. 31 (2019) 1706825.
[69] F. Luo, F. Jaouen, P. Strasser, et al., Nat. Mater. 19 (2020) 1215–1223.
[70] Y. Li, L. Dai, Y. Hou, et al., Angew Chem. Int. Ed. 60 (2021) 9078–9085.